

# Perfect flat band and chiral-charge ordering out of strong spin-orbit interaction

Hiroki Nakai\* and Chisa Hotta

*Department of Basic Science, University of Tokyo, Meguro-ku, Tokyo 153-8902, Japan<sup>†</sup>*

(Dated: December 24, 2024)

Spin-orbit interaction established itself as a major role player for emergent phenomena in modern condensed matter including a topological insulator, spin liquid and spin-dependent transports. However, its function is rather limited to adding topological nature to each phases of matter. We prove by our spinor line graph theory that a very strong spin-orbit interaction realized in  $5d$  pyrochlore electronic systems generates multiply degenerate perfect flat bands. Unlike any of the previous flat bands, the electrons living there localize in real space by destructively interfering with each other in a spin selective manner ruled by the  $SU(2)$  gauge field. These electrons avoid the Coulomb interaction by self-organizing their localized wave functions. This gives rise to the trimerized charge ordering hand in hand with a stiff spin chirality, which may explain the recently found exotic low-temperature insulating phase of  $CsW_2O_6$ .

## I. INTRODUCTION

Electronic flat bands in momentum space is an ideal platform for realizing the strongest correlation in a zero-bandwidth-limit<sup>1-3</sup>. A long history tells us that such flat bands naturally arise in a class of geometrically frustrated lattices like kagome, pyrochlore, and checkerboard lattices, which are well understood based on the line graph theory and its analogs<sup>4</sup>. Recently, the importance of having flat bands in real correlated materials is focused in twisted bilayer graphene<sup>5-7</sup>, where the relationship between superconductivity and magnetism have been extensively discussed. On top of finely tuning a magic 'twisting' angle, the flat bands arise by structurally introducing a pseudo magnetic field onto graphene layer<sup>8</sup>.

There is another trend to add some topological nature to these flat bands<sup>9-11</sup>, expecting an emergent fractional quantum Hall states without a magnetic field, as they have a nonzero Chern number and mimic the Landau levels. A small spin-orbit coupling (SOC) helps to systematically realize a series of such nearly flat bands<sup>12</sup>, which are experimentally observed in kagome lattice materials like  $CoSn$ <sup>13</sup> and twisted multilayer silicene<sup>14</sup>. Unfortunately, all these examples show that the perfect flatness of the bands are sacrificed to make up for topological properties<sup>15</sup>.

Indeed, SOC rather enhances the itinerancy of electrons, and its major role had been to introduce some topological nature to the kinetic motion of particles. In SOC electronic systems<sup>16-18</sup>, Berry phase is introduced to the energy bands, which became an important source of spin-dependent transports like anomalous Hall effect<sup>19</sup> and spin Hall effect<sup>20-23</sup>. Surface states of topological insulators<sup>24,25</sup> are the Dirac state that is another distinct feature of energy bands induced by the weak SOC. When strong electronic interactions are introduced, these topological band insulators are transformed to the topological Mott insulator marked with gapless surface spinon excitations<sup>26</sup>. A very strong SOC creates more exotic phases modifying the form of quasi-particles in Kitaev magnets<sup>27</sup>, i.e. a spin liquid<sup>28</sup> hosting Majorana fermions

and antiferromagnets with topological magnons<sup>29,30</sup>. Despite all these hallmark studies, there had been no example that the SOC gives a direct impact on the electronic correlation effect.

Here, we prove analytically that the SOC induced spin-dependent hopping which previously made the bands dispersive perfectly flattens the energy bands of the pyrochlore and kagome lattices when it becomes comparably as large as the transfer integrals. Most importantly, the SOC generates an  $SU(2)$  gauge field<sup>31</sup> and strictly selects the relative angles of electronic spins to destructively interfere<sup>32</sup> their wave functions and makes them localized in real space. The analytical many body flat band wave function give access to the important but the most unreachable physical regime, the effectively strongest correlation, where they optimize their form in a way to avoid the loss of the Coulomb energy. This mechanism explains the exotic trimerized charge ordering found in  $5d$  pyrochlore  $CsW_2O_6$ <sup>33</sup>, where one-quarter of the pyrochlore sites become perfectly vacant. On each triangle, there appears a stiff spin chirality inextricably linked to the flat band formation, which may provide another platform for testing the interplay of strong correlation and spin topology.

## II. MODEL SYSTEM

We introduce a minimal microscopic model for the  $5d$  pyrochlore oxides<sup>34</sup> with  $CsW_2O_6$  as a specific example. A metallic  $W^{5.5+}$  ion on a pyrochlore lattice is surrounded by a slightly distorted oxygen octahedron, and its electronic state is understood by considering the lowest Kramers doublet of this ion ( $E_2$  in Fig.1(a)) which carries the momentum  $J_{eff} = 3/2$ ,  $J_{eff}^z = \pm 1/2$ , and comes out as the mixtures of  $t_{2g}$  triplet after considering the strong spin-orbit coupling (SOC) typical of the  $5d$  electrons in a trigonal crystal field<sup>35</sup>. In the present quarter-filled case, the doublet carries 0.5 electrons on an average, where the energy levels  $E_1 - E_2 \sim 200meV$  are well separated(see AppendixA). For such doublet with momentum  $1/2$  described by the pseudo-spins,  $\alpha = \uparrow, \downarrow$ ,

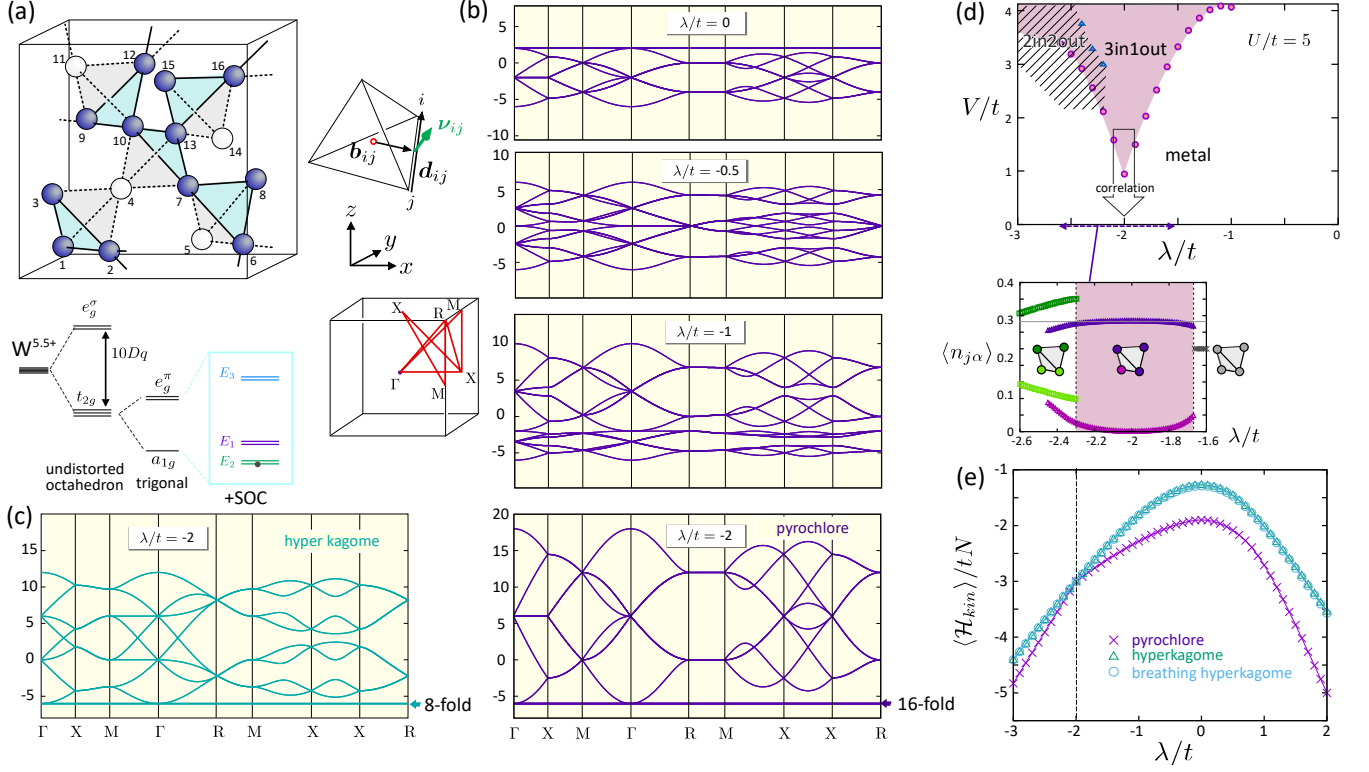


FIG. 1. (a) Unit cell of the pyrochlore/hyperkagome lattice based on the  $W$ -ions. Filled and open circles represent the occupied and unoccupied sites in the trimerized charge order phase of  $\text{CsW}_2\text{O}_6$ , where the former forms a hyper kagome lattice.  $\mathbf{b}_{ij}$  and  $\mathbf{d}_{ij}$  are vectors defined for bond  $i$ - $j$ , determining the form of the SOC. Energy levels of single  $W$ -ion surrounded by the oxygen ligand. (b) Noninteracting band structure (Eq.(C1) with  $U = V = 0$ ) of the pyrochlore lattice for  $\lambda/t = 0, -0.5, -1, -2$ . The  $k$ -paths are chosen as in the left side panel. (c) Noninteracting band structure of the hyperkagome lattice obtained by depleting  $1/4$  of the lattice sites from the pyrochlore lattice with  $\lambda/t = -2$ . (d) Mean field phase diagram of Eq.(C1) on the plane of  $\lambda/t$  and  $V/t$  for  $U/t = 5$ . Circles/triangles represent the boundary where the energy of the 3-in-1-out becomes lower than the metallic state and 2-in-2-out state, respectively. When we consider the exact many body flat wave function, the energy of 3-in-1-out is lowered by the mean field on-site Coulomb energy  $\sim U/12$  and the phase boundary collapses to  $V/t = 0$ . (inset) Charge density  $\langle n_{j\uparrow} \rangle = \langle n_{j\downarrow} \rangle$  of charge rich and poor sites at  $V/t = 3$  of the mean-field solution. (e) Noninteracting band energy  $\langle \mathcal{H}_{kin} \rangle / tN$  of the pyrochlore, hyperkagome, and the breathing hyper kagome lattices.

the conventional the Hubbard type of Hamiltonian<sup>36</sup> is written as a sum of hopping terms with spatially uniform transfer integral  $t$  and Coulomb interaction  $V$  between the nearest neighbor sites,  $\langle i, j \rangle$ , as well as the on-site  $U$ :

$$\begin{aligned} \mathcal{H} &= \mathcal{H}_{kin} + \mathcal{H}_I, \\ \mathcal{H}_{kin} &= \sum_{\langle i, j \rangle} \sum_{\alpha, \beta} (-t \delta_{\alpha\beta} c_{i\alpha}^\dagger c_{j\beta} + i \lambda c_{i\alpha}^\dagger (\mathbf{v}_{ij} \cdot \boldsymbol{\sigma})_{\alpha\beta} c_{j\beta}) + \text{h.c.}, \\ \mathcal{H}_I &= \sum_j U n_{j\uparrow} n_{j\downarrow} + \sum_{\langle i, j \rangle} V n_i n_j, \end{aligned} \quad (1)$$

where  $c_{j\alpha}$  annihilates an electron with pseudospin  $\alpha$  at site- $j$ , and  $n_{j\alpha}$  and  $n_j = n_{j\uparrow} + n_{j\downarrow}$  are their number operators. The bare atomic SOC which may possibly amount to  $\zeta \sim 200 - 300$  meV manifests itself as the spin-dependent hopping  $\lambda$ , where the vector  $\mathbf{v}_{ij}$  gives the coefficients of the Pauli matrices,  $\boldsymbol{\sigma} = (\sigma_x, \sigma_y, \sigma_z)$ , which is bond-dependent and is determined by the crystal symmetry. For the uniform pyrochlore lattice, we find  $\mathbf{v}_{ij} = \sqrt{2} \frac{\mathbf{b}_{ij} \times \mathbf{d}_{ij}}{|\mathbf{b}_{ij} \times \mathbf{d}_{ij}|}$  with  $\mathbf{b}_{ij}$  and  $\mathbf{d}_{ij}$  being the vectors

pointing from the center of the tetrahedron to the bond center, and along the bond, respectively (see Fig.1(a)). (see Appendix A)<sup>37</sup>. The mean field phase diagram of Eq.(C1) at half-filling is studied for Ir-oxides<sup>38</sup> showed that the strong SOC generates a series of phases from a topological band insulator, a topological semimetal to a topologically nontrivial Mott insulator in increasing  $U$ . There, the overall evolution of energy band structures in varying  $\lambda/t$  and  $U/t$  are also studied in the context of finding a good Weyl point at the middle of levels<sup>36,39</sup>. In the present work, we notice that the SOC can drive another exotic phenomenon, a perfect flat band and a resultant trimerized charge ordering supported by the stiff chirality of pseudo spins.

Let us first set  $\mathcal{H}_I = 0$  and write down the energy bands by varying  $\lambda/t$  in Fig.1(b). One finds a perfect flat band at the bottom when  $\lambda/t = -2$ . There is another case with a flat band at the top when  $\lambda/t = 0$ , which is the typical one known from the line-graph geometry. Usually, introducing the SOC is known to de-

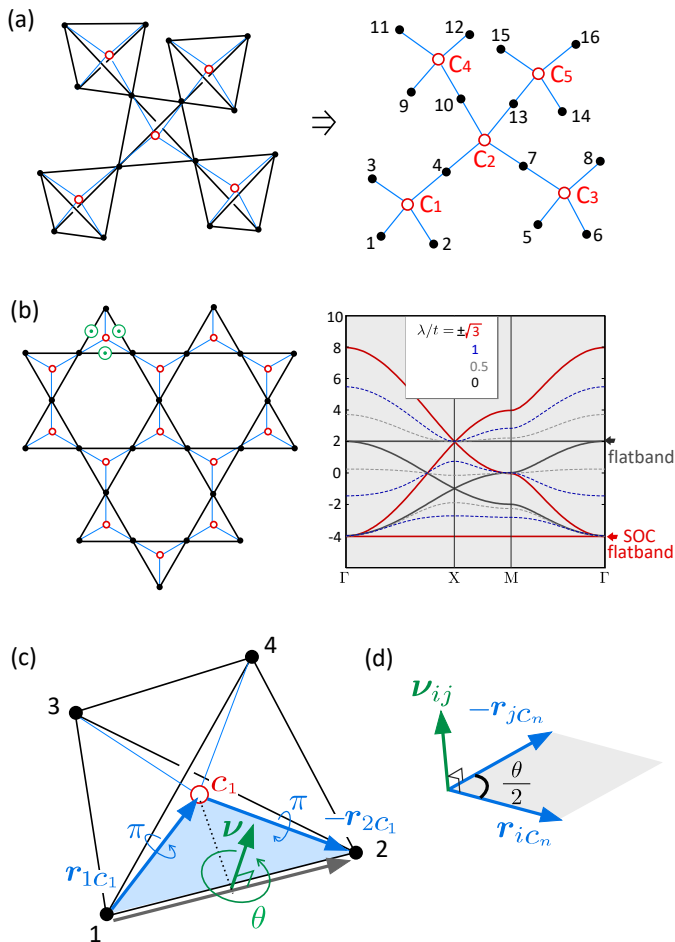


FIG. 2. (a) Pyrochlore lattice and its dual diamond lattice ( $C_j$ ) in red circle. The two lattices are connected and form a linegraph on the right panel. (b) Kagome and its dual honeycomb lattice, where  $\mathbf{v}_{ij} = (0, 0, \pm 1)$ . Noninteracting and structures for  $\lambda/t = 0 - \sqrt{3}$  are shown. (c) Unit tetrahedron. Hopping  $1 \rightarrow 2$  rotates the spin orientation by  $-\theta$  about the  $\mathbf{v}_{12}$ -axis, whereas hopping through  $1 \rightarrow C_1 \rightarrow 2$  rotates the spin orientation twice by  $\pi$  each about the  $\mathbf{r}_{1C_1} = (1, -1, 1)$  and  $\mathbf{r}_{2C_1} = (-1, 1, 1)$  axes for site-1 and 2 in Fig.1(a). (d) Condition to have SOC flat band in Eq.(7).

stroy the perfectness of this top flat band<sup>12</sup> as one can see for the case of  $\lambda/t = -0.5$ , or similarly the perfect flat band cannot have nonzero Chern number<sup>15</sup>. Notice that among the 32 bands, half contribute to the top flat band at  $\lambda/t = 0$  which gradually gains the bandwidth by  $\lambda < 0$ , while at the same time the other dispersive half starts to shrink and finally become perfectly flat at  $\lambda/t = -2$ . We also show in Fig.1(c) the band structure of the hyper kagome lattice at the same  $\lambda/t = -2$ , obtained by depleting 1/4 of the pyrochlore sites, where we also find an 8-fold degenerate flat band at the same location.

### III. RESULTS

#### A. Phase diagram

The SOC-induced flat band clarifies the origin of the trimerized charge ordering observed in  $\text{CsW}_2\text{O}_6$ <sup>33</sup>. Figure 1(d) shows the mean field phase diagram at quarter-filling, corresponding to two electrons per tetrahedron. We treat the Coulomb interaction terms  $\mathcal{H}_I$  as Hartree-types of mean-field, and denote the solutions with  $n$ -charge rich sites per tetrahedron as  $n$ -in-(4- $n$ )-out. The trivial paramagnetic metallic state with uniform charge and spin distribution are dominant when the Coulomb interaction is small. The distinct feature is the emergent 3-in-1-out state extending at around  $\lambda/t = -2$ , which has 2/3 electrons per hyperkagome site, keeping 1/4 of the site almost perfectly empty (see the inset of Fig.1(d)). The 2-in-2-out phase with about 0.35 : 0.15 charge disproportionation is stabilized only at  $\lambda/t \lesssim -2$ .

The reason why 3-in-1-out is stable is understood clearly by comparing the band energies  $\langle \mathcal{H}_{kin} \rangle$  in Fig.1(e) when the pyrochlore and hyper-kagome lattices host  $8N_c$  electrons, where  $N_c$  is the number of the unit cell. The band energy gain is always the largest for the pyrochlore lattice with a larger coordination number giving the largest bandwidth, and indeed, the  $\lambda > 0$  region of the phase diagram is dominated by the trivial metallic phase even when introducing a relatively large  $U$  and  $V$ . However, at  $\lambda/t = -2$ , the pyrochlore and hyper kagome band energies become degenerate because all the electrons fill the bottom flat band which appears in both cases. The mean field interaction energy is roughly evaluated by hand, which is  $E_I^{metal} = U + 12V$  and  $E_I^{3i1o} = 4U/3 + 32V/3$  per unit cell for metal and 3-in-1-out, respectively, which is consistent with our numerical evaluation based on mean-field(see Appendix B). Then, the introduction of  $V/t \gtrsim 1$  stabilizes the 3-in-1-out state over the metallic phase. We show later on that the 3-in-1-out state does not feel the on-site Coulomb energy  $U$  when the quantum many body correlation is fully included.

#### B. Spinor line graph theory

The perfect flat band at  $\lambda/t = -2$  cannot be explained within any of the previous frameworks. Here, we develop a spinor line graph theory to prove the existence of the SOC-induced flat bands, which can be applied to general line-graph-based lattices. To this end, we first overview the flat band theory on line graphs. Figures 2(a)-(b) show the relationships between the original lattice and its dual lattice described by red circles. The dual lattice of the pyrochlore lattice is the diamond lattice, and by connecting the pyrochlore and diamond sites and deleting the pyrochlore bonds, one reaches the bipartite line graph. The same relationship holds between the kagome-honeycomb lattices. The real space matrix representa-

tion of the tight binding model of the line graph consists of two off-diagonals blocks as,

$$\hat{H}_{lg} = \begin{pmatrix} 0 & T_{OD} \\ T_{DO} & 0 \end{pmatrix} \quad (2)$$

where  $T_{OD} = {}^{t*}T_{DO}$  is the  $N \times N_D$  matrix with  $N = 16N_c$  and  $N_D = 8N_c$  being the number of pyrochlore and diamond lattice sites, respectively, where  $(T_{OD})_{ij} = 1$  for the  $i$ -th pyrochlore and  $j$ -th diamond sites connected by blue bonds and zero otherwise. Since the matrix representation of the tight binding Hamiltonian of the pyrochlore lattice is written as,

$$\hat{H}_{\text{pyrochlore}}(\lambda = 0) = 2t\hat{I} - tT_{OD}T_{DO}, \quad (3)$$

the  $N$ -dimensional vector  $\varphi_l$  that fulfills  $T_{DO}\varphi_l = 0$ , i.e. the kernel  $\{\varphi_l\}$ , also satisfies  $\hat{H}_{\text{pyrochlore}}\varphi_l = 2t\varphi_l$ . Since the dimension of the kernel is at least  $N - N_D (> 0)$ , there exists at least  $(N - N_D)/N_c = 8$  flat bands in the pyrochlore lattice with energy  $2t$ , which is the one found in Fig.1(b) at  $\lambda/t = 0$ , where considering the spin degeneracy, the number of flat band is doubled.

The extension of the line graph theory to  $\lambda \neq 0$  is not straightforward, since the hopping term rewritten as

$$\mathcal{H}_{kin} = \sum_{\langle i,j \rangle} -\sqrt{t^2 + 2\lambda^2} c_i^\dagger U_{ij} c_j, \quad U_{ij} = e^{-i\frac{\theta}{2}\hat{\nu}_{ij}\cdot\sigma}, \quad (4)$$

includes the non-Abelian SU(2) gauge field  $U_{ij}$ <sup>31</sup>, where  $\mathbf{c}_j = (c_{j\uparrow}, c_{j\downarrow})$  and  $\hat{\nu} = \boldsymbol{\nu}/|\boldsymbol{\nu}|$  is the unit vector. The gauge field along  $j \rightarrow i$  gives the SU(2) spin rotation about the  $\boldsymbol{\nu}_{ij}$ -axis by the angle  $\theta = -\arctan(\sqrt{2}\lambda/t)$ . We want to replace this complex hopping with the fictitious hoppings from pyrochlore  $i$ -th site to diamond and to pyrochlore  $j$ -th site; In introducing the SU(2) gauge, the tetrahedral symmetry only allows us to use the rotational axes parallel to these paths pointing from the edge to the center of the tetrahedron, which we denote as  $\mathbf{r}_{iC_j}$ . We show the example in Fig.2(d), where one easily finds that the only way to retain the rotation axes as  $\boldsymbol{\nu}_{12}$  by the combination of the rotations about  $\mathbf{r}_{1C_1}$  and  $\mathbf{r}_{2C_1}$ -axes is to have both rotation angles  $\pi$ , namely  $i\hat{\mathbf{r}}_{1C_1} \cdot \boldsymbol{\sigma} = \exp(-i(\pi/2)\hat{\mathbf{r}}_{1C_1} \cdot \boldsymbol{\sigma})$ . Then, we are able to prepare the transfer matrix  $\tilde{T}_{OD}$  for  $\lambda \neq 0$  consisting of SU(2) gauges as,

$$(\tilde{T}_{OD})_{iC_j} = \begin{cases} i(\mathbf{r}_{iC_j} \cdot \boldsymbol{\sigma}) & \text{(connected by line graph)} \\ 0 & \text{(otherwise)} \end{cases} \quad (5)$$

which has twice as large dimension as  $T_{OD}$ , and fulfills  $\tilde{T}_{DO} = {}^{t*}\tilde{T}_{OD}$ . We set the length of vectors along the blue linegraph bonds as  $|\mathbf{r}_{iC_j}| = \sqrt{3}$ . The modified form of Eq.(3) becomes

$$\hat{H}_{\text{pyrochlore}}(\lambda/t = -2) = -6t\hat{I} - t\tilde{T}_{OD}\tilde{T}_{DO}, \quad (6)$$

which holds when and only when  $\lambda/t = -2$ . There, we find  $2(N - N_D)/N_c = 16$  flat bands at the energy bottom  $-6t$ .

The same discussion holds for the kagome and hyper kagome lattices. As shown in Fig.2(c) the usual  $\lambda = 0$ -flat band of the kagome lattice at  $+2t$  starts to gain bandwidth with  $\lambda \neq 0$ , while the dispersive bottom band shrinks and become the SOC flat band at  $-4t$  when  $\lambda = \pm\sqrt{3}$ . (See Appendix C for details).

The general strategy to design such SOC flat band is quite simple. The dual lattice sites  $C_n$  is set to have the Wilson loop operator around the closed loop  $i \rightarrow C_n \rightarrow j$ , lose its phase factor. In our case,  $\mathcal{A}_{1C_12} = U_{1C_1}U_{C_12}U_{21} = e^{-\pi/2\hat{\mathbf{r}}_{1C_1}\cdot\boldsymbol{\sigma}}e^{-\pi/2\hat{\mathbf{r}}_{C_12}\cdot\boldsymbol{\sigma}}e^{-i\frac{\theta}{2}\hat{\nu}_{12}}$  equals to 1. For that, one needs to choose  $C_n$  so that the cross product  $\mathbf{r}_{iC_n} \times \mathbf{r}_{jC_n}$  be parallel to  $\boldsymbol{\nu}_{ij}$ . The parameter values that yield the SOC flat band is given as (see Fig.2(d))

$$\frac{|\mathbf{r}_{iC_n} \times (-\mathbf{r}_{jC_n})|}{\mathbf{r}_{iC_n} \cdot (-\mathbf{r}_{jC_n})} = \tan \frac{\theta_{ij}}{2} = -\frac{\lambda|\boldsymbol{\nu}_{ij}|}{t}. \quad (7)$$

This means that for the two dimensional lattices, the SOC vector  $\boldsymbol{\nu}$  shall point in the out-of-plane direction, and also when  $\theta = \pi$ , the  $ij$ -bond takes  $t = 0$  and  $\lambda \neq 0$  which is often unphysical. For this reason, the edge shared lattices like square, checkerboard, and honeycomb lattices are excluded from the realistic example.

### C. Destructive interference

Although treating the model beyond the mean-field level is too challenging in general, our case is exceptional since the zero-bandwidth at  $\lambda = -2t$  practically corresponds to the strong coupling limit which can be treated analytically. Among the one body flat bands orbitals,  $\varphi_{l\alpha}$  ( $l = 1, \dots, 16N_c, \alpha = \uparrow, \downarrow$ ), half are filled. The shapes of the one-body flat band wave functions can be chosen as their linear combinations, such that they minimize the interaction energy loss in all. This context is in analogy with the flat band ferromagnetism of the Hubbard model<sup>1,2</sup>, which is realized in a way that the electrons polarize and avoid each other in space by making use of Pauli's principle.

The  $m$ -th one-body eigen state of  $\mathcal{H}_{kin}$  is written as  $|\psi_m\rangle = \sum_{j,\alpha} \varphi_{j\alpha}^m c_{j\alpha}^\dagger |0\rangle$ , where the complex coefficients  $\varphi_{j\alpha}^m$  are the elements of  $32N_c$ -dimensional flat band vector  $\tilde{\varphi}_m$  that fulfills  $\tilde{T}_{DO}\tilde{\varphi}_m = 0$ . This condition is read so as to prohibit the net propagation to all the diamond sites  $n = 1, \dots, N_D$  respectively from their adjacent four pyrochlore sites which we write as  $j \in n$ ;

$$\sum_{j \in n} i\mathbf{r}_{jC_n} \cdot \boldsymbol{\sigma} \begin{pmatrix} \varphi_{j\uparrow}^m \\ \varphi_{j\downarrow}^m \end{pmatrix} = 0. \quad (8)$$

In visualizing this, we first set the fictitious SU(2) spinor  $\boldsymbol{\chi}_n$  (two dimensional vector) at the  $n$ -th tetrahedron center pointing somewhere as in Fig.3(a). Suppose that the four adjacent pyrochlore orbitals have their spins point in the directions rotated by  $\pi$  about their respective axes

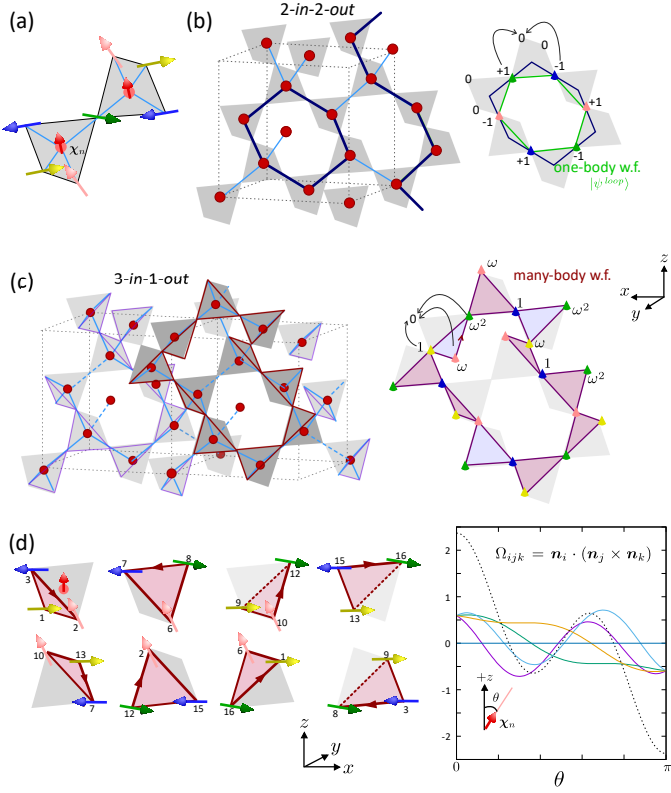


FIG. 3. (a) Relative spin configuration of the flat band states. Spins on the edges of the tetrahedra are created from the center spin (red arrow) via  $SU(2)$ -rotation by  $\pi$  about the axes pointing from the center toward the edge. The orientation of fictitious spins at the center of the two adjacent tetrahedra,  $C_i$  and  $C_j$ , point in the same direction as far as they are connected by the finite population of spins at the edge between  $C_i$  and  $C_j$ . (b) Schematic illustration of the *one-body* flat band wave function forming a loop. The tetrahedra belonging to the loop has the *2-in-2-out* configuration. The weights of electrons on these sites have the staggered arrangement  $+1, -1, \dots$ , and the spins are oriented in the directions marked with different colors, which are relatively fixed. (c) Schematic illustration of the *many body* flat band wave function, which is factorized into the set of one-body operators on each triangle forming a *3-in-1-out* structure. The weights of electrons on three sites ( $1, \omega, \omega^2$ ) are canceled out when they hop to the remaining one site of the tetrahedron, since they fulfill the condition Eq.(8). (d) Four different directions of spins marked with different colors, which form eight different types of triangles in the many body flat band wave function. The solid angle is evaluated for four pairs of triangles separately as a function of angle  $\theta$  about the  $+z$ -direction, and its summation given in broken line takes the maximum amplitude for  $\theta = 0, \pi$ .

from this fictitious spinor. If some of their  $\varphi_{j\alpha}^m$  ( $j \in n$ ) are finite, one needs to cancel them out on a whole by adjusting their values using Eq.(8). Since the spin shared by the two tetrahedra should fulfill the condition for both, and since it follows the same  $\pi$ -rotation axis for both, the adjacent fictitious spins point in the same direction

as far as they are connected by the finite pyrochlore sites with nonzero weight in the wave function. One example of  $|\psi_m\rangle$  is given as such that they form a closed loop consisting of an even number of bonds, shown in Fig.3(b). By putting  $+1$  and  $-1$  weights alternatively along the loop while fixing their spin direction in a way that they are rotated by  $\pi$  about their corresponding  $r_{iC_n}$ -axis from the fictitious center spin, a single electron is perfectly localized on the loop. This is because if they want to hop outside the loop, they are canceled out, which is the physical meaning of the destructive interference<sup>32</sup> or the kinetic frustration. The one-body form of the flat band wave function is valid only when electrons are dilute.

In the present case, we need to put two electrons per tetrahedron. Even in such case, we succeeded in constructing the *many body flat band wave function* in a factorized form,  $|\Psi_{3in1out}\rangle \propto \prod_{n \in \text{hyperkagome}} \hat{\psi}_n^{tri}|0\rangle$ , using a single electron operator on a triangular unit of the hyperkagome lattice,  $\hat{\psi}_n^{tri} = \sum_{i \in n} \eta_i (\mathbf{e}_i^\dagger i \mathbf{r}_{iC_n} \cdot \boldsymbol{\sigma}) \chi_n$ , as building blocks. By choosing the phase factor  $\eta_i = 1, \omega, \omega^2$ , with  $\omega = e^{i2\pi/3}$  properly, Eq.(8) is satisfied. The schematic illustration is given in Fig.3(c). Notice that all tetrahedra have  $\chi_n$  pointing in the same direction, and join this wave function. The triangles are colored according to the clockwise and counter-clockwise way of assigning the phase factors. While both equally fulfill Eq.(8), we need to mix both types, since setting all the triangles clockwise will make the above product form of  $|\Psi_{3in1out}\rangle$  exactly zero because of the fermionic anticommutation relation. We can easily find that the *2-in-2-out* type of many body wave function factorized into bond operators always becomes zero and cannot be constructed. This is consistent with our mean field results showing that the *3-in-1-out* has the almost perfect exclusion of occupancy on the charge poor site but the *2-in-2-out* does not.

A notable feature of this flat band state is that it perfectly avoids the double occupancy of electrons, which yields  $\langle \Psi_{3in1out} | U n_{i\uparrow} n_{i\downarrow} | \Psi_{3in1out} \rangle = 0$ . Accordingly, the interaction energy is much smaller than the mean field *3-in-1-out* solution, shifting the phase boundary to  $V/t = 0$  in Fig.1(d). The electrons on a flat band thus could maximally avoid the electronic correlation, making use of the degrees of freedom of forming a wave function out of numerous choices.

One can rotate the fictitious spinor  $\chi_n$  or fluctuate them to have a nonmagnetic ground state or finite temperature state. Even in such case, the constituents of the many body flat band state exactly keeps the relative angles of the spins on triangles fixed, which indicates the stiff chiral ordering. As shown in Fig.3(d) there are eight species of triangles in a unit cell, whose spin orientations are shown for the case where the fictitious spinor points in the  $+z$ -direction. If we consider that these pseudo-spins suffer the magnetic field generated by the  $SU(2)$  gauge field, its flux equals half of the solid angle  $\Omega_{ijk}$  subtended the spin directions around the triangle. We evaluated  $\Omega_{ijk} = \mathbf{n}_i \cdot (\mathbf{n}_j \times \mathbf{n}_k)$  for four independent triangles in Fig.3(d) as a function of angle  $\theta$  of the ficti-

tious spinor about the  $+z$ -axis. We define a unit vector  $\mathbf{n}_j$  parallel to the pseudo spins with the right hand rule about  $+z$ -axis. At  $\theta = 0, \pi$  we find maximum amplitude,  $\Omega_{321} = \pm 16/27$ . In this case, this scalar chirality contributes to the  $xy$ -component of the anomalous thermal Hall conductivity for insulators or it might affect  $\sigma_{xy}$  for metals<sup>40,41</sup>.

#### IV. SUMMARY AND DISCUSSION

Concerning the experimental findings, the important question is whether the actual material parameters really fit to our scenario. It is known that the  $5d$  electrons are more extended in space with a reduced values of on-site Coulomb repulsion  $U \sim 1 - 2\text{eV}^5$  and the extended bandwidth, which may favor a metallic state<sup>34,42</sup>. However, a large atomic SOC,  $\zeta$ , usually dominates the  $t_{2g}$  orbitals and splits them into higher  $J_{\text{eff}} = 1/2$  doublet and lower  $3/2$  quartet, and in our case the lowset doublet coming out from the quartet with  $J_{\text{eff}}^z = \pm 1/2$  is focused (see Fig.1(a)).

The present value of  $\zeta \sim 200 - 300\text{meV}$  is about half of the reference materials in  $5d$  Iridates that the SOC has comparably large or much larger value than the transfer integrals, e.g. a Mott insulating  $\text{Sr}_2\text{IrO}_4$  is reported to have  $t \sim 0.3\text{eV}$  and  $\zeta \sim 0.5\text{eV}^{43}$ , the parameters of the honeycomb Kitaev material  $\text{Na}_2\text{IrO}_3$  evaluated from the first principles as  $t \sim 0.27\text{eV}$  and  $\zeta \sim 0.39\text{eV}^{44}$ . The distortion angle of the octahedron is  $55.7^\circ$ , only slightly larger than the regular octahedron  $54.74^\circ$ , which may not alter the form of the  $\lambda$ -term which assumed the regular pyrochlore structure. Still, the evaluated energy splitting of  $E_1 - E_2 \sim 0.2\text{eV}$  is as large as the bandwidth of our system (see Appendix A), which is compatible with the first principles band structure given in Ref.[33] where we roughly evaluate  $t \sim 0.06\text{eV}$  by their bandwidth.

The  $t_{2g}$  orbital momentum  $\mathbf{L}^{\text{eff}} = 1$  resembles the  $p$ -orbital representation with its sign taken as minus, where we find  $\mathbf{J}_{\text{eff}} = -\mathbf{L}^{\text{eff}} + \mathbf{S}$  as good quantum numbers<sup>37</sup>. Then, the magnetic moment  $\mathbf{M} = 2\mathbf{S} - \mathbf{L}^{\text{eff}}$  becomes zero for the undistorted octahedron, while for the present case the admixture of levels coming from small trigonal distortion gives finite moment  $\langle M_z \rangle$  still as small as  $1/5$  of that of the full moment of electron, while it is difficult to compare this directly with the available experimental results. In the low temperature phase II, we expect the trimer flat band state, which has a Mott gap. This explains the sharp increase of the resistivity at the transition temperature<sup>33</sup>. There shall be a stiff pseudo-spin chirality formed by a tiny magnetic moment, indicating that the system breaks the time reversal symmetry. However, the nature of this chirality is different from the usual magnetic ordering in that it cannot shrink freely with the external field as far as it belongs to the many body flat band state, since the orientation of the pseudo-spin is locked, for which we expect a finite spin gap. Although the precise evaluation of  $\lambda$  of  $\text{CsW}_2\text{O}_6$  are not available at

present, it should be negative and be comparably as large as  $t$ , because this value comes from the hoppings between  $|a_{1g}\rangle$  and  $|e_g^\pi\rangle$  with the same positive coefficients. We also notice that one does not need strictly  $\lambda/t = -2$  to have a trimerization, as the phase diagram shows that there is some sort of pinning effect to the flat bands when the electronic interactions are finite.

Before the recent discovery of trimerized charge ordering that keeps the Anderson condition<sup>33</sup>,  $\text{CsW}_2\text{O}_6$  was considered to undergo a Peierls-type of metal-insulator transition<sup>45</sup>. This was partially because the DFT calculation showed a large enhancement of the density of states near the Fermi level<sup>46</sup>, which was ascribed to the electronically driven structural-metal-insulator transition into the possible zig-zag-like one-dimensional structure. Other first principles calculation supported this picture arguing that the SOC enhances the nesting instability<sup>47</sup>. In revisiting these works, the enhanced density of states may well explain the possible SOC induced flat band, which may not be perfect in nature, but would be enough to drive the system to the trimerized charge ordering. According to our theory, this charge order is different from the conventional ones driven mostly by the Coulomb interaction  $V$ . The interplay of SOC and transfer integral is its main source.  $U$  and  $V$  only helps to indirectly support it since they have the advantage over trivial phases in that they could self-organize themselves rather freely within the flat band manifold to get the optimal configuration of charges to avoid these Coulomb interactions.

The present picture might be examined by the anomalous thermal Hall measurement in the insulating phase or the anomalous Hall electronic transport in the metallic state. In the previously known cases of the intrinsic anomalous Hall effect, often the SOC acting on the conducting electrons on a dispersive band<sup>41</sup> or the localized moments working as spatially coplanar internal field onto the conducting electrons<sup>40</sup> was considered as a source of the emergent gauge field. In our case, the SOC is playing a more crucial role, as it works to kill their momentum  $k$  and strictly selects the orientation of pseudo-spin moments with negligibly small true moments that may virtually propagate in space since it is on a flat band. It is thus beyond the scope of the present transport theories on how such features may appear in the transport phenomena and will provide another playground for SOC.

#### Appendix A: Atomic levels of $5d$ materials

We consider the atomic level of  $5d$  electrons with in mind the W-atoms of  $\text{CsW}_2\text{O}_6$  forming a pyrochlore lattice following Ref.[35]. The W-atom is surrounded by an oxygen octahedron. The octahedron is slightly distorted in a manner to compress the octahedron in a trigonal manner. The degree of distortion is measured by the

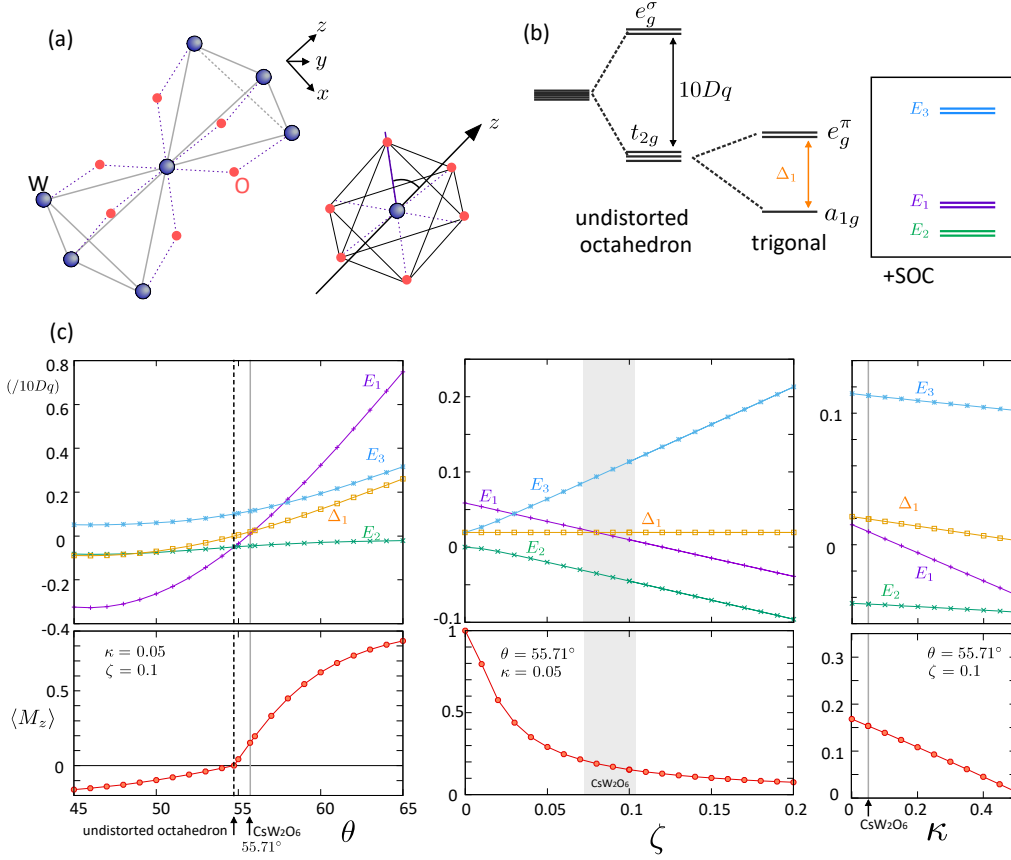


FIG. 4. (a) Pyrochlore lattice consisting of W-atoms and the surrounding oxygen octahedron (red circle). (b) Crystal field splitting including the spin-orbit coupling  $\zeta$ . (c) Energy levels  $E_1 - E_3$  under finite  $\zeta$  and trigonal distortions, crystal field splitting  $\Delta_1$  and the magnetic moment  $\langle M_z \rangle$  evaluated for the lowest doublet.

angle  $\theta$ , where we take the local  $z$ -axis of the octahedron with trigonal symmetry as those pointing perpendicular to the faced triangles. From the single crystal XRD data in Ref.[33], we evaluate the angle  $\theta = 55.71^\circ$  for 250K (phase I), which is only slightly larger than  $\theta_0 = 54.74^\circ = \arccos(1/\sqrt{3})$  of the undistorted octahedron.

In a octahedral crystal field, the  $5d$  levels split into higher  $e_g^\sigma$  doublet and lower  $t_{2g}$ -triplets, which for the trigonal crystal field further split into  $a_{1g}$  singlet and  $e_g^\pi$  doublet (see Fig.4(b)). Using the coordinate shown in Fig.4(a), these  $t_{2g}$  functions are given for each effective angular momentum  $L_z^{eff}$  as,

$$\begin{aligned}
 |a_{1g}\rangle &= |x^2 - y^2\rangle & L_z^{eff} &= 0, \\
 |e_{g1}^\pi\rangle &= (i|g_1\rangle - |g_2\rangle)/\sqrt{2} & L_z^{eff} &\sim +1, \\
 |e_{g2}^\pi\rangle &= (i|g_1\rangle + |g_2\rangle)/\sqrt{2} & L_z^{eff} &\sim -1, \\
 |g_1\rangle &= -\cos\frac{\alpha}{2}|xy\rangle + \sin\frac{\alpha}{2}|yz\rangle, \\
 |g_2\rangle &= \cos\frac{\alpha}{2}|x^2 - y^2\rangle + \sin\frac{\alpha}{2}|x\rangle,
 \end{aligned} \tag{A1}$$

where  $\alpha$  and  $\theta$  are related by the following equation;

$$\begin{aligned}
 \cos\alpha &= \frac{a}{a^2 + b^2}, \tag{A2} \\
 a &= \frac{27}{35}\kappa(3\cos^2 - 1) - \frac{3}{2}\left(\frac{5}{2}\cos^4\theta - \frac{15}{7}\cos^2\theta + \frac{3}{14}\right), \\
 b &= 3\sin^3\cos^2\theta. \tag{A3}
 \end{aligned}$$

The energy difference between  $|e_{g1}^\pi\rangle$  and  $|a_{1g}\rangle$  levels are given by  $\Delta_1 = \sqrt{a^2 + b^2}$  which is determined by the distortion angle  $\theta$  and  $\kappa$ .

The introduction of large spin-orbit interaction  $\zeta \mathbf{l} \cdot \mathbf{s}$  mixes these  $a_{1g}$  and  $e_g^\pi$  levels, which leads to three doublets with energy  $E_1, E_2$  and  $E_3$ . Their energies and effective angular momentum  $J_{eff}$  are given for the combination of  $t_{2g}$  levels and electron spins  $\sigma = \uparrow, \downarrow$  as

$$\begin{aligned}
 E_1 &= 2(\Delta_1 - \Delta), \\
 E_2 &= \Delta - \sqrt{\Delta^2 + \xi^2}, \\
 E_3 &= \Delta + \sqrt{\Delta^2 + \xi^2}, \\
 \Delta &= \frac{\Delta_1}{2} + \frac{1 + 3\cos\alpha}{8}\zeta, \quad \xi = \sqrt{\frac{3}{2}}\sin\frac{\alpha}{2}\zeta,
 \end{aligned} \tag{A4}$$

where the corresponding wave functions  $|\phi_\sigma^{(i)}\rangle$  for dou-

plets  $i = 1 - 3$  are

$$\begin{aligned}
|\phi_{\uparrow}^{(1)}\rangle &= |e_{g1}^{\pi}; \uparrow\rangle, \quad |\phi_{\downarrow}^{(1)}\rangle = |e_{g1}^{\pi}; \downarrow\rangle \quad (J_{eff} = \frac{3}{2}, J_{eff}^z = \pm \frac{3}{2}) \\
|\phi_{\uparrow}^{(2)}\rangle &= \cos \delta |a_{1g}; \uparrow\rangle + \sin \delta |e_{g1}^{\pi}; \downarrow\rangle \\
|\phi_{\downarrow}^{(2)}\rangle &= \cos \delta |a_{1g}; \downarrow\rangle + \sin \delta |e_{g1}^{\pi}; \uparrow\rangle \quad (J_{eff} = \frac{3}{2}, J_{eff}^z = \pm \frac{1}{2}) \\
|\phi_{\uparrow}^{(3)}\rangle &= \sin \delta |a_{1g}; \uparrow\rangle - \cos \delta |e_{g1}^{\pi}; \downarrow\rangle \\
|\phi_{\downarrow}^{(3)}\rangle &= \sin \delta |a_{1g}; \downarrow\rangle - \cos \delta |e_{g1}^{\pi}; \uparrow\rangle \quad (J_{eff} = \frac{1}{2}, J_{eff}^z = \pm \frac{1}{2})
\end{aligned} \tag{A5}$$

We are interested in the case where the  $E_2$ -doublet becomes the lowest in energy where maximally one electron occupies this level. Since these doublets carry magnetic moment coming originally from the  $J_{eff} = 3/2$  quartet, where we can evaluate the net magnetic moment as  $\mathbf{M} = 2\mathbf{S} - \mathbf{L}^{eff}$  where  $\mathbf{L}^{eff}$  is the effective momentum the  $t_{2g}$  orbitals carry, one can evaluate the magnetic moment of the  $E_2$ -doublet as

$$|\langle M_z \rangle| = \cos^2 \delta - \sin^2 \delta \left( 1 + \left( 2 \cos^2 \frac{\alpha}{2} - \sin^2 \frac{\alpha}{2} \right) \right), \tag{A6}$$

where  $L^{eff} = 2 \cos^2 \frac{\alpha}{2} - \sin^2 \frac{\alpha}{2}$  becomes  $\pm 1$  for the undistorted octahedron.

To see how much extent this situation can be realized, we plot in Fig.4(c) the energy levels  $E_1 \sim E_3$ ,  $\Delta_1$  and  $\langle M_z \rangle$  (for the lowest energy level) by varying  $\theta$ ,  $\zeta$  and  $\kappa$ . Here, we take the crystal field splitting between the  $e_g$  and  $t_{2g}$  orbitals,  $10Dq \sim 3eV$ , as an energy unit. Since the SOC of W-ions are considered to be more than half of those of Iridates, namely  $200 - 300meV$ , we consider  $\zeta \sim 0.06 - 0.1$ .

The value of  $\kappa$  is evaluated by considering the integral  $\kappa = r_0^2 \langle r^2 \rangle / \langle r^4 \rangle$  with  $\langle r^n \rangle = \int_0^\infty r^n R_d^2(r) r^2 dr$  and  $R_d(r) \sim r^3 \exp(-z^* r / 4a_B)$  for  $5d$  electrons. Here we take the W-O distance  $r_0 \sim 1.95\text{\AA}$  and the Slater's rule  $z^* = 6$  ( $z = 74$  for W-atom). This gives  $\kappa \sim 0.05$ .

One sees that the magnetic moment is suppressed to about 0.1-0.2 from the full magnetic moment of electrons  $g\mu_B/2$  for the material parameters of  $CsW_2O_6$ . Also the energy difference between the  $E_2$  and higher  $E_1$  is about  $0.055/(10Dq) \sim 0.2$  eV, which is quite larger than the transfer integral  $t \sim 0.06$  eV evaluated separately from the band structural calculation. Since we are dealing with the bottom energy level with no band dispersion, our approximation of taking only the lowest  $E_2$ -doublet is verified.

## Appendix B: Details of the mean field solution

We examined the competition between the metallic solution with uniform charge density  $\langle n_{j\alpha} \rangle \sim 0.25$  ( $\alpha = \uparrow, \downarrow$ ), 3-*in-1-out* solution with three charge rich sites located on the hyper-kagome site  $\langle n_{j\alpha} \rangle \sim 1/3$ , and 2-*in-2-out* solution having two charge rich sites  $\langle n_{j\alpha} \rangle \sim 0.35$

and two charge poor sites  $\langle n_{j\alpha} \rangle \sim 0.15$  per tetrahedron. The obtained energy per site  $E/N$  at  $U/t = 5$  are plotted for these solutions in Fig.5(a),(b). Particularly, the uniform metallic solution follows  $E_{uniform}/tN = e_{pyro}/t + U/16t + 3V/4t$ , obtained by hand where  $e_{pyro}$  is the band energy of the noninteracting pyrochlore lattice at  $U = V = 0$  which is shown together in lines to compare with the mean field data points. The 3-*in-1-out* and 2-*in-2-out* solutions also show clear linear  $V/t$  dependences which are fitted by the following functions,

$$E/(tN) = e_{\phi}/t + a_{\phi}V/t, \quad \phi = 3in1out, 2in2out. \tag{B1}$$

These coefficients are shown in Fig.5(c). Here, the notable feature is that the effective noninteracting band energies of 2-*in-2-out* state,  $e_{2in2out}$  resembles those of the band energy of the hyperkagome lattice rather than the stripe solution. Also the  $V/t$  dependence of  $a_{3in1out}$  goes to  $2/3$  which is expected for the perfect flat band solution where we have  $2/3$  charges per triangular sites and  $3/2$  bonds per site which gives  $(2/3)^2 \times (3/2) = 2/3$ . Although this value linearly increases off this value, the mean field solution is found to work very well to describe the 3-*in-1-out* flat band state since the charge density does not change much over a wide parameter range  $-2.2 \leq \lambda/t \leq -1.8$ .

## Appendix C: Spinor line graph theory for the kagome lattice and some comments

We consider the Hamiltonian with transfer integral  $t$  and spin-orbit interaction  $\lambda$ ,

$$\mathcal{H}_{kin} = \sum_{\langle i,j \rangle} \sum_{\alpha,\beta} (-t \delta_{\alpha\beta} c_{i\alpha}^{\dagger} c_{j\beta} + i\lambda c_{i\alpha}^{\dagger} (\boldsymbol{\nu}_{ij} \cdot \boldsymbol{\sigma})_{\alpha\beta} c_{j\beta}) + \text{h.c.}, \tag{C1}$$

where we set  $t = 1$  and take

$$\boldsymbol{\nu}_{ij} = \frac{\mathbf{b}_{ij} \times \mathbf{d}_{ij}}{|\mathbf{b}_{ij} \times \mathbf{d}_{ij}|}, \tag{C2}$$

where notice that the factor differs by  $\sqrt{2}$  from that of the main text for pyrochlore lattice. For the kagome lattice we find  $\boldsymbol{\nu}_{ij} = (0, 0, \pm 1)$ . We consider  $N_c$  unit cells where each unit cell includes three sites. The dual lattice is the honeycomb lattice with two sites per cell given in open red circles in Fig.6(a). From the conventional line graph theory, the kagome band for  $\lambda = 0$  has a flat band at the top level,  $+2t$ ;  $2N_c \times 3N_c$  matrix  $T_{DQ}$  has two 1's on each column, which gives  $T_{OD}T_{DO} = 2\hat{I} - \hat{H}_{kagome}/t$ . The kernel  $\{\boldsymbol{\varphi}\}$  which fulfills  $T_{DO}\boldsymbol{\varphi} = \mathbf{0}$  has the dimension  $3N_c - 2N_c = N_c$ , and this gives a single flat band.

The extension to  $\lambda \neq 0$  requires the elements of the above matrix to be replaced by twice the large one as

$$(\tilde{T}_{OD})_{ic_j} = \begin{cases} i(\mathbf{r}_{iC_j} \cdot \boldsymbol{\sigma}) & (\text{connected by linegraph}) \\ 0 & (\text{otherwise}) \end{cases} \tag{C3}$$

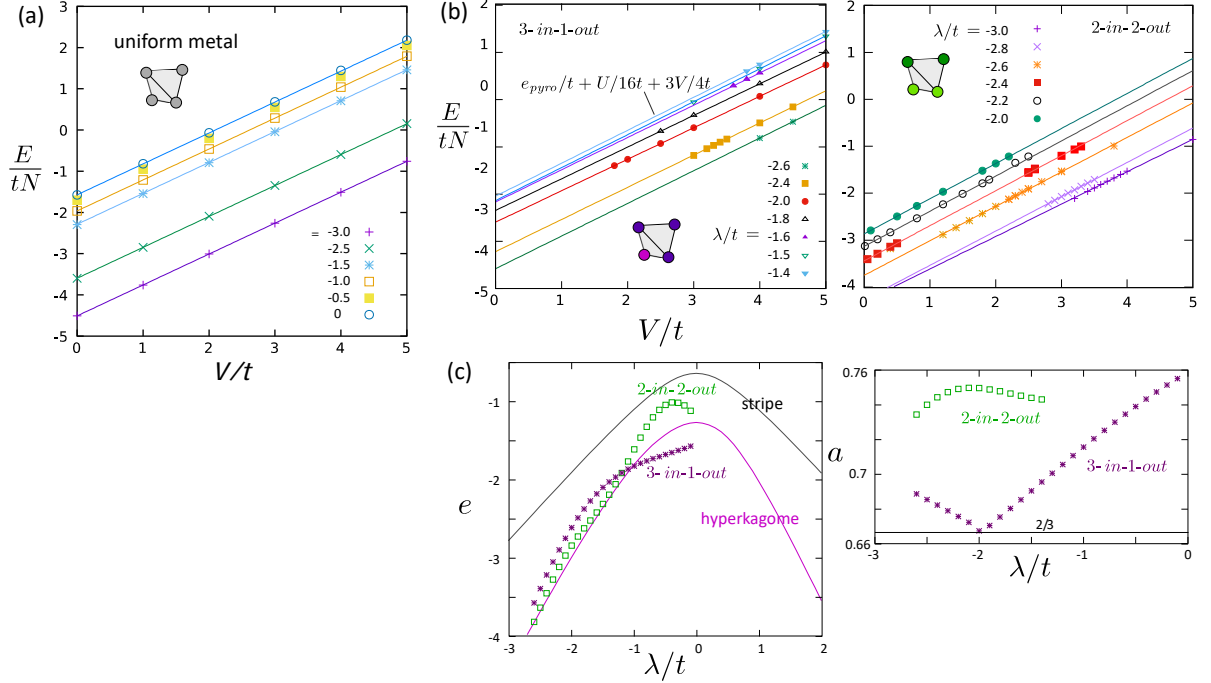


FIG. 5. (a) Energy per site of the uniform metallic mean field solution, which follows  $E/N = e_{pyro}/t + U/16t + 3V/4t$ . Here,  $e_{pyro}$  as a function of  $\lambda/t$  is given in Fig.1 in the main text. (b) Energy per site of the 3-in-1-out and 2-in-2-out solutions, fitted via Eq.(B1). (c) Results of fitting given in panel (b),  $e_\phi$  and  $a_\phi$ , together with the noninteracting band energy of the hyperkagome and stripe states in solid lines for comparison.

with  $\mathbf{r}_{1C_1} = (\sqrt{3}/2, 1/\sqrt{2}, 0)$ ,  $\mathbf{r}_{2C_1} = (-\sqrt{3}/2, 1/\sqrt{2}, 0)$  and  $\mathbf{r}_{3C_1} = (0, -\sqrt{2}, 0)$  shown in Fig.6(a). Since  $(i\mathbf{r}_{1C_1} \cdot \boldsymbol{\sigma}) \cdot (-i\mathbf{r}_{1C_2} \cdot \boldsymbol{\sigma}) = \hat{I} - \sqrt{3}i\sigma_z$  and  $(i\mathbf{r}_{1C_1} \cdot \boldsymbol{\sigma}) \cdot (-i\mathbf{r}_{1C_1} \cdot \boldsymbol{\sigma}) = -2\hat{I}$ , we obtain the relationship

$$\tilde{T}_{OD}\tilde{T}_{DO} = -4\hat{I} - \hat{H}_{\text{kagome}}(\lambda/t = -\sqrt{3})/t.$$

Since the sign of  $\lambda$  does not change the nature of the system, we find the SOC flat band at  $-4t$  when  $\lambda/t = \pm\sqrt{3}$ , which is demonstrated in Fig.2.

The SOC induced flat band of the hyperkagome lattice has the construction almost the same as the pyrochlore one. One only needs to deplete 1/4 of the lattice sites and the same formulation applies.

We also show in Fig.7(a)-(c) the examples of lattices where the present spinor line graph is difficult to apply. In these cases, the angles formed by the two  $\mathbf{r}_{iC_n}$  vectors take  $\theta/2 = \pi/2$ , which requires  $t = 0$  along the bonds while keeping  $\lambda \neq 0$ , when the flat band is realized. Also, the edge shared lattices cannot have the SOC pointing perpendicular to the two dimensional plane. The next nearest neighbor SOC, fulfilling  $\lambda = \sqrt{3}t$  can be realized on the honeycomb lattice in Fig.S7(c), but at the same time  $\lambda = \sqrt{3}/2t$  is required along the honeycomb bonds which is not possible, since  $\lambda = 0$ .

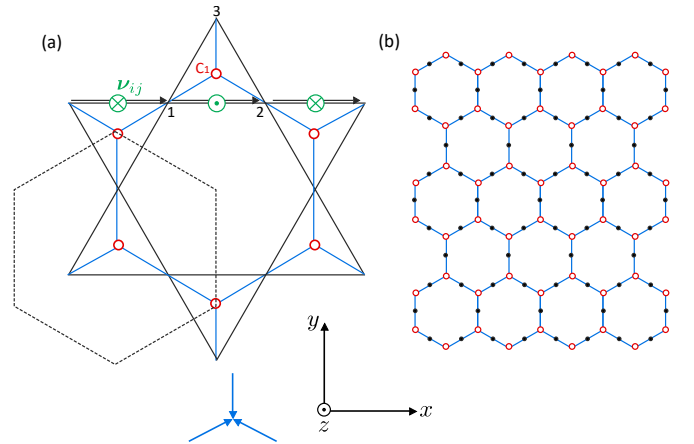


FIG. 6. (a) Kagome lattice and (b) its line graph consisting of the dual honeycomb lattice (red open circle) and the kagome lattice (bullet) sites.

## ACKNOWLEDGMENTS

We thank Taka-hisa Arima, Yoshihiko Okamoto, Youichi Yamakawa and Masataka Kawano for discussions. The work is supported by JSPS KAKENHI Grants No. JP17K05533, No. JP18H01173, No. JP17K05497.

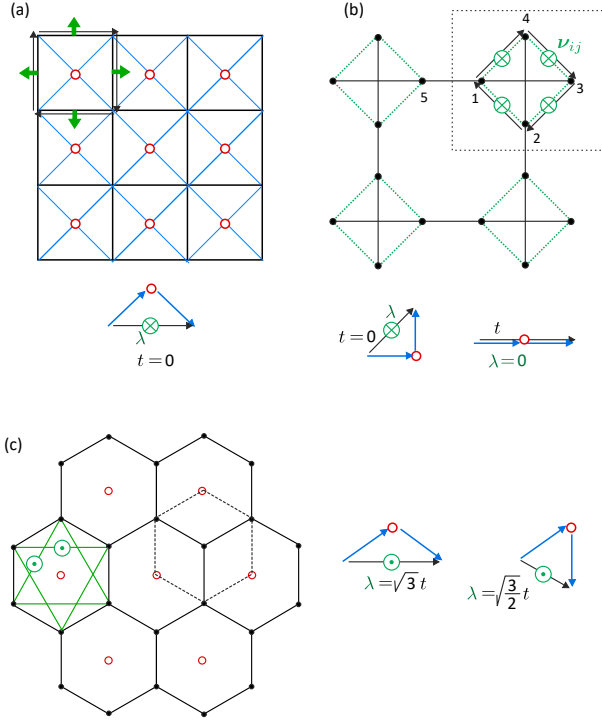


FIG. 7. Example of lattices which the SOC flat band is not easy to realize. (a) Square lattice, (b) Square-octagon lattice and (c) honeycomb lattice. Lower panels are the constructions of  $r_{iC_n} \rightarrow r_{jC_n}$  which gives the necessary condition for  $\lambda/t$  about the realization of the flat band. For  $\theta/2 = \pi/2$  in cases like (a) and (b),  $t = 0$  is required which is unrealistic. For the honeycomb lattice, the SOC along the nearest neighbor honeycomb bonds are usually zero, which does not fulfill the condition  $\lambda = \sqrt{3/2}t$  in the right panel.

\* nakai-hiroki3510@ecc.u-tokyo.ac.jp

† chisa@phys.c.u-tokyo.ac.jp

<sup>1</sup> A. Mielke, J. Phys. A: Math. Gen. **24**, 3311 (1991).

<sup>2</sup> H. Tasaki, Phys. Rev. Lett. **69**, 1608 (1992).

<sup>3</sup> A. Mielke and H. Tasaki, Commun. Math. Phys. **158**, 341 (1993).

<sup>4</sup> S. Miyahara, K. Kubo, H. Ono, Y. Shimomura, and N. Furukawa, J. Phys. Soc. Jpn. **74**, 1918 (2005).

<sup>5</sup> Y. Cao, V. Fatemi, S. Fang, K. Watanabe, T. Taniguchi, E. Kaxiras, and P. Jarillo-Herrero, Nature **556**, 215 (2018).

<sup>6</sup> Y. Xie, B. Lian, B. Jäck, X. Liu, C.-L. Chiu, K. Watanabe, T. Taniguchi, B. A. Bernevig, and A. Yazdani, Nature **572**, 101 (2019).

<sup>7</sup> X. Lu, P. Stepanov, W. Yang, M. Xie, M. A. Aamir, I. Das, C. Urgell, K. Watanabe, T. Taniguchi, G. Zhang, A. Bachtold, A. H. MacDonald, and D. K. Efetov, Nature **574**, 653 (2019).

<sup>8</sup> J. Mao, S. P. Milovanović, M. Anelković, X. Lai, Y. Cao, K. Watanabe, T. Taniguchi, L. Covaci, F. M. Peeters, A. K. Geim, Y. Jiang, and E. Y. Andrei, Nature **584**, 215 (2020).

<sup>9</sup> E. Tang, J.-W. Mei, and X.-G. Wen, Phys. Rev. Lett. **106**, 236802 (2011).

<sup>10</sup> K. Sun, Z. Gu, H. Katsura, and S. Das Sarma, Phys. Rev. Lett. **106**, 236803 (2011).

<sup>11</sup> T. Neupert, L. Santos, C. Chamon, and C. Mudry, Phys. Rev. Lett. **106**, 236804 (2011).

<sup>12</sup> D.-S. Ma, Y. Xu, C. S. Chiu, N. Regnault, A. A. Houck, Z. Song, and B. A. Bernevig, Phys. Rev. Lett. **125**, 266403 (2020).

<sup>13</sup> M. Kang, S. Fang, L. Ye, H. C. Po, J. Denlinger, C. Jozwiak, A. Bostwick, E. Rotenberg, E. Kaxiras, J. G. Checkelsky, and R. Comin, Nat. Commun. **11**, 4004 (2020).

<sup>14</sup> Z. Li, J. Zhuang, L. Wang, H. Feng, Q. Gao, X. Xu, W. Hao, X. Wang, C. Zhang, K. Wu, S. X. Dou, L. Chen, Z. Hu, and Y. Du, Sci. Adv. **4** (2018), 10.1126/sciadv.aau4511.

<sup>15</sup> A. Chen, L. Mazaheri, T. Seidel and X. Tang, J. Phys. A: Math. and Theor. **47**, 152001 (2014).

<sup>16</sup> E. I. Rashba, Sov. Phys. Solid State **2**, 1224 (1960).

<sup>17</sup> R. C. Casella, Phys. Rev. Lett. **5**, 371 (1960).

<sup>18</sup> G. Dresselhaus, Phys. Rev. **100**, 580 (1955).

- <sup>19</sup> R. Karplus and J. M. Luttinger, *Phys. Rev.* **95**, 1154 (1954).
- <sup>20</sup> S. Murakami, N. Nagaosa, and S.-C. Zhang, *Science* **301**, 1348 (2003).
- <sup>21</sup> J. Sinova, D. Culcer, Q. Niu, N. A. Sinitsyn, T. Jungwirth, and A. H. MacDonald, *Phys. Rev. Lett.* **92**, 126603 (2004).
- <sup>22</sup> Y. K. Kato, R. C. Myers, A. C. Gossard, and D. D. Awschalom, *Science* **306**, 1910 (2004).
- <sup>23</sup> J. Wunderlich, B. Kaestner, J. Sinova, and T. Jungwirth, *Phys. Rev. Lett.* **94**, 047204 (2005).
- <sup>24</sup> C. L. Kane and E. J. Mele, *Phys. Rev. Lett.* **95**, 146802 (2005).
- <sup>25</sup> B. A. Bernevig, T. L. Hughes, M. Kang, and S.-C. Zhang, *Science* **314**, 1757 (2006).
- <sup>26</sup> D. Pesin and L. Balents, *Nat. Phys.* **6**, 376 (2010).
- <sup>27</sup> G. Jackeli and G. Khaliullin, *Phys. Rev. Lett.* **102**, 017205 (2009).
- <sup>28</sup> J. G. Rau, E. K.-H. Lee, and H.-Y. Kee, *Annu. Rev. Condens. Matter Phys.* **7**, 195 (2016).
- <sup>29</sup> P. A. McClarty, X.-Y. Dong, M. Gohlke, J. G. Rau, F. Pollmann, R. Moessner, and K. Penc, *Phys. Rev. B* **98**, 060404(R) (2018).
- <sup>30</sup> M. Kawano and C. Hotta, *Phys. Rev. B* **100**, 174402 (2019).
- <sup>31</sup> S.-S. Zhang, H. Ishizuka, H. Zhang, G. B. Halász, and C. D. Batista, *Phys. Rev. B* **101**, 024420 (2020).
- <sup>32</sup> N. Hatano, R. Shirasaki, and H. Nakamura, *Phys. Rev. A* **75**, 032107 (2007).
- <sup>33</sup> Y. Okamoto, H. Amano, N. Katayama, H. Sawa, K. Niki, R. Mitoka, H. Harima, T. Hasegawa, N. Ogita, Y. Tanaka, M. Takigawa, Y. Yokoyama, K. Takehana, Y. Imanaka, Y. Nakamura, H. Kishida, and K. Takenaka, *Nat. Commun.* **11**, 3144 (2020).
- <sup>34</sup> W. Witczak-Krempa, G. Chen, Y. B. Kim, and L. Balents, *Annu. Rev. Condens. Matter Phys.* **5**, 57 (2014).
- <sup>35</sup> K. I. Kugel, D. I. Khomskii, A. O. Sboychakov, and S. V. Streltsov, *Phys. Rev. B* **91**, 155125 (2015).
- <sup>36</sup> M. Kurita, Y. Yamaji, and M. Imada, *J. Phys. Soc. Jpn.* **80**, 044708 (2011).
- <sup>37</sup> B. J. Kim, H. Jin, S. J. Moon, J.-Y. Kim, B.-G. Park, C. S. Leem, J. Yu, T. W. Noh, C. Kim, S.-J. Oh, J.-H. Park, V. Durairaj, G. Cao, and E. Rotenberg, *Phys. Rev. Lett.* **101**, 076402 (2008).
- <sup>38</sup> W. Witczak-Krempa and Y. B. Kim, *Phys. Rev. B* **85**, 045124 (2012).
- <sup>39</sup> W. Witczak-Krempa, A. Go, and Y. B. Kim, *Phys. Rev. B* **87**, 155101 (2013).
- <sup>40</sup> G. Tatara and H. Kawamura, *J. Phys. Soc. Jpn.* **71**, 2613 (2002).
- <sup>41</sup> S. Onoda, N. Sugimoto, and N. Nagaosa, *Phys. Rev. Lett.* **97**, 126602 (2006).
- <sup>42</sup> T. Takayama, J. Chaloupka, A. Smerald, G. Khaliullin, and H. Takagi, (2021), preprint at <https://arxiv.org/abs/2102.02740>.
- <sup>43</sup> J. Dai, E. Calleja, G. Cao, and K. McElroy, *Phys. Rev. B* **90**, 041102 (2014).
- <sup>44</sup> Y. Yamaji, Y. Nomura, M. Kurita, R. Arita, and M. Imada, *Phys. Rev. Lett.* **113**, 107201 (2014).
- <sup>45</sup> T. Soma, K. Yoshimatsu, K. Horiba, H. Kumigashira, and A. Ohtomo, *Phys. Rev. Materials* **2**, 115003 (2018).
- <sup>46</sup> D. Hirai, M. Bremholm, J. M. Allred, J. Krizan, L. M. Schoop, Q. Huang, J. Tao, and R. J. Cava, *Phys. Rev. Lett.* **110**, 166402 (2013).
- <sup>47</sup> S. V. Streltsov, I. I. Mazin, R. Heid, and K.-P. Bohnen, *Phys. Rev. B* **94**, 241101 (2016).